



Selective ozone catalyzation modulated by surface and bulk oxygen vacancies over MnO_2 for superior water purification

Liying Wu^a, Zonglin Wang^a, Jiaye Liu^a, Caihong Liu^b, Xueyan Li^c, Yixuan Zhang^d, Wei Wang^a, Jun Ma^a, Zhiqiang Sun^{a,*}

^a State Key Laboratory of Urban Water Resource and Environment, School of Environment, Harbin Institute of Technology, Harbin 150090, PR China

^b Key Laboratory of Eco-environments in Three Gorges Reservoir Region, Ministry of Education, College of Environment and Ecology, Chongqing University, Chongqing 400044, PR China

^c School of Environmental Science and Engineering, Suzhou University of Science and Technology, Suzhou 215009, PR China

^d Shanghai Municipal Engn Design & Res Inst Grp Co, Shanghai 200090, PR China

ARTICLE INFO

Keywords:

Oxygen vacancy

Spatial position

Selective catalytic ozonation

Hydroxy radical

Electron transfer process

ABSTRACT

The regulation behavior of oxygen vacancies (Vo) at different spatial positions (surface or bulk) in catalysts for selective O_3 catalyzation, along with the reaction pathways evolution was well-investigated in $\alpha\text{-MnO}_{2-x}/\text{O}_3$ systems. Combined characterization methods, systematic organic removal experiments, structure-activity relationship analysis, and theoretical calculations were employed to unveil O_3 decomposition and electron transfer behaviors regulated by surface or bulk Vo. The contribution of electron transfer process (ETP) to atrazine (ATZ) removal was reinforced from 5.2 % to 34.8 % with the formation of bulk Vo, and Vo-rich $\alpha\text{-MnO}_{2-x-2}/\text{O}_3$ system achieved ~96.5 % ATZ removal along with improved TOC mineralization (~38 % vs. ~20 %). Surface Vo facilitated O_3 adsorption, promoting its decomposition into $\bullet\text{OH}$, while bulk Vo not only accelerated $\bullet\text{OH}$ production but also withdrew electrons from organics to build ETP. This study shed light on precise modification of metal-based catalysts with Vo to modulate $\bullet\text{OH}$ /ETP synergistic processes in catalytic ozonation for efficient water purification.

1. Introduction

Ozone (O_3), known for its strong oxidation capacity, is commonly used in practical water treatment to efficiently remove organics [1,2]. However, the chemical inertness of O_3 molecules toward saturated bonds hinders the complete mineralization of degradation intermediates [3]. Recent advancements in catalytic ozonation, attributed to the generation of various and abundant reactive oxygen species (ROSs), have demonstrated superiority over conventional ozonation for organic mineralization [4–9]. In this case, the effective utilization of O_3 with catalysts is of great importance for catalytic processes. Metal-based catalysts (e.g., Mn^{2+} , Co^{2+} , Fe^{3+} , Fe_3O_4 , MgO , MnO_2 , Co_3O_4) have emerged as promising candidates for catalytic ozonation due to their natural abundance and high efficiency in producing ROSs [4,10,11]. Nevertheless, metal-based catalytic ozonation processes remain challenges: i) the scarcity of active sites (surface hydrogen groups, Lewis acid and Brønsted acid sites) per unit area in metal-based catalysts is adverse to the electronic properties utilization of metal redox sites, limiting full

play of the reactive activity; ii) since active sites predominantly concentrate on catalysts surface, an excess of ROSs is produced instantaneously at the initial stage of the catalytic ozonation process, leading to a severe self-quenching phenomenon and reduced stoichiometry efficiency; iii) the reusability of metal-based catalysts is severely hampered due to the easy passivation of the active sites at the catalytic interface by the sluggish kinetics of metal redox recycling [12]. To address these issues, extensive research efforts have focused on developing novel, effective metal-based catalysts by fabricating and exposing the utmost catalytic active sites [13], triggering various activation pathways, and inducing efficient metal redox cycling.

Recently, various efficient approaches, such as hybridization, heterointerface and defect engineering [14,15], have been exploited to achieve the required targets (e.g., excellent catalytic performance and improved reusability). Among these techniques, defects (point, line, planar and volume defects) fabrication, emerged as the distortion of the periodic structure of the crystal, is a novel and effective strategy to modulate the active sites and metal redox cycling performance [16].

* Corresponding author.

E-mail address: sunhit@hit.edu.cn (Z. Sun).

<https://doi.org/10.1016/j.apcatb.2023.123526>

Received 11 September 2023; Received in revised form 9 November 2023; Accepted 13 November 2023

Available online 15 November 2023

0926-3373/© 2023 Elsevier B.V. All rights reserved.

One of the typical point defects with the lowest formation energy is native oxygen vacancies (Vo), which can be easily constructed and are generally accepted as the most effective modification method to boost catalytic performance [17]. Vo possess the ability to both accept and donate electrons, thereby building electron transfer channels throughout catalysts [18–21]. In this regard, in addition to their potential role as catalytic active sites, Vo, which integrated into the crystalline structure of metal-based materials, can also simultaneously modulate the inherent electronic configuration, ultimately promoting the exposure of catalytic sites. Likewise, Vo can also alleviate catalysts passivation due to their superior electron transfer property, facilitating the redox cycle of metals. Most importantly, Vo can induce some other extraordinary pathways, including $^1\text{O}_2$, $\text{O}_2^{\bullet-}$, and electron transfer process (ETP) [22,23], not limited to the $\bullet\text{OH}$. Thus, the introduction of Vo becomes a rational strategy to break through the bottleneck of self-consumption of ROSS during catalytic processes [18,24,25]. Besides, catalytic ozonation is a three-phase catalytic system, in which the proper affinity, reactivity and mass transport at solid-liquid-gas interface are distinguished as the decisive role in regulating catalytic efficiency and O_3 utilization [26,27]. Vo, due to their high surface energy, can reduce the activity of the oxygen exchange “surface”, potentially promoting the adsorption of H_2O and O_3 onto the catalytic surface [27–29]. Therefore, Vo construction is a versatile strategy to effectively address the above-summarized shortages of metal-based materials and significantly reduces the energy threshold of reactions at the solid-liquid-gas interface in catalytic ozonation.

However, the specific mechanisms regulated by Vo in metal-based catalysts during catalytic ozonation still remain insufficient and subject to controversy [18,27,28,30]. Some studies clarified that the Vo in metal-based catalysts primarily function as adsorption sites for O_3 to accelerate the subsequent electrophilic reaction with metal active centers, resulting in the formation of $\bullet\text{OH}$ [18]. Nevertheless, others proposed that Vo may serve as intrinsic active sites within metal-based catalysts, generating $\text{O}_2^{\bullet-}$, $^1\text{O}_2$, or inducing ETP pathway in catalytic ozonation [21,27]. Notably, previous studies have often overlooked a key information: different spatial positions of Vo (surface Vo and bulk Vo) play distinct roles in catalytic processes [30,31]. This oversight has contributed to significant disagreements regarding the identification of active sites and catalytic pathways in Vo-involved catalytic ozonation. Researchers have identified the diverse roles of Vo in the bulk and surface of catalysts in catalytic combustion [32] and photocatalysis [31]. Unfortunately, the in-depth understanding of the Vo, which govern different catalytic mechanisms, is rarely studied and remains ambiguous in catalytic ozonation. This makes the promotion of Vo on the catalytic performance (e.g., selectively, reactive activity, and stoichiometry efficiency) become very random in catalytic ozonation. Thus, it is imperative to unravel the relationship between Vo structures and catalytic performance to provide criteria for the precise modification of metal-based catalysts for superior catalytic ozonation.

For the first time, our research modified the surface and bulk of the simple monometallic oxide $\alpha\text{-MnO}_2$ with Vo, revealing the different roles of Vo located at different spatial positions in enhancing the efficiency of catalytic ozonation, as well as the underlying regulatory mechanism regarding reactive activity and stoichiometry efficiency during organics elimination. Firstly, the typical organics degradation in $\alpha\text{-MnO}_2\text{-x}/\text{O}_3$ systems was comprehensively investigated along with activity assessment, selectivity evaluation, identification of catalytic active centers and ROSSs, Vo evolution, and organics elimination pathways. Then, the diverse roles of Vo at different spatial positions in relation to O_3 decomposition were unveiled by combined characterization methods, structure-activity relationships analysis, and density functional theory (DFT) calculations. Finally, a novel catalytic ozonation mechanism was proposed for organics elimination using Vo-rich metal-based catalysts. This fundamental study holds great significance in the development of efficient and practical metal-based catalytic ozonation systems for superior water purification.

2. Materials and methods

2.1. Chemicals and reagents

Potassium permanganate (KMnO_4), ammonium oxalate monohydrate ($(\text{NH}_4)_2\text{C}_2\text{O}_4\cdot\text{H}_2\text{O}$), and atrazine (ATZ) were purchased from Aladdin Co. Ltd. More details are listed in the Text S1. All chemicals and reagents were used as received without further purification.

2.2. Catalyst preparation and characterization

The Vo-modified $\alpha\text{-MnO}_2$ including $\alpha\text{-MnO}_{2-x}$, $\alpha\text{-MnO}_{2-x-0.5}$, $\alpha\text{-MnO}_{2-x-1}$, $\alpha\text{-MnO}_{2-x-2}$ and $\alpha\text{-MnO}_{2-x-3}$ were successfully synthesized by hydrothermal and H_2 calcination method (0, 0.5, 1, 2, 3 h), as displayed in Text S2. Systematic characterization methods (Text S3) were applied to investigate the morphology, structure, Vo formation and evolution, adsorption performance, and electron transfer property of catalysts. The quantitative analysis of Vo was also conducted by iodometric titration method (Text S4). In situ linear sweep voltammetry and Raman spectroscopy, and X-ray photoelectron spectroscopy (XPS) were further used to investigate the interfacial reaction process and redox process in catalytic ozonation (Text S5).

2.3. Experimental procedures

Ozonation/catalytic ozonation experiments were conducted in a 1.5 L glass reactor equipped with a magnetic stirrer at a stirring speed of 300 rpm. O_3 was produced by an O_3 generator (Xiamen Laisen Electronics Co., LTD, China) with ultrapure oxygen (99.9 %) as the gas source. The inlet flow rate of O_3 was control at 100 mL/min and fed from the bottom of the reactor by a glassy porous diffuser, detailed experimental set-up is shown in Text S6 and Fig. S1. Other details of experimental procedures are given in Text S7.

2.4. Computational methodology

Density functional theory calculations were performed using Vienna ab initio Simulation Package (VASP) within generalized gradient approximation (GGA) [33,34]. The Perdew-Burke-Ernzerhof (PBE) functionals were used for the exchange-correlation potential and the Projector Augmented Wave (PAW) pseudo potentials were adopted [35, 36], detail calculation methods are shown in Text S8.

3. Results and discussion

3.1. Morphology and structure of Vo-rich $\alpha\text{-MnO}_{2-x}$

A series of Vo-modified monometallic MnO_{2-x} were obtained through calcination under H_2 atmosphere for varying durations. All Vo-modified $\alpha\text{-MnO}_{2-x}$ samples manifested as clusters of nanowires with diameters of 10–20 nm [27,37] and the interplanar distance was ~ 0.320 nm along the growth axis, corresponding to the (310) facet of $\alpha\text{-MnO}_{2-x}$ (Fig. 1a and Figs. S2–3). It was consistent with the X-ray diffraction (XRD) results of $\alpha\text{-MnO}_{2-x}$ samples (Text S9 and Fig. S4). As reported [27,38], the $\alpha\text{-MnO}_{2-x}$ (310) had remarkable activity and required lower energy for Vo formation. And the small diameter of $\alpha\text{-MnO}_{2-x}$ nanowires was beneficial to the exposure of more Vo sites in $\alpha\text{-MnO}_{2-x}$. Electron paramagnetic resonance (EPR) spectroscopy was employed to analyze the Vo content of $\alpha\text{-MnO}_{2-x}$. It could be obtained that $\alpha\text{-MnO}_{2-x}$ with longer calcination time displayed a stronger symmetrical signal intensity ($g=2.003$), which positively associated with Vo concentration. It indicated that prolonging the treatment time was beneficial for Vo formation, and the H_2 atmosphere was more favorable for Vo formation compared to N_2 (Fig. 1b). The increased disordered structure (Fig. 1a and Fig. S3c) and decreased O atom content (60 % vs 40 %, Fig. S5a-b) with prolonged treatment time further confirmed the

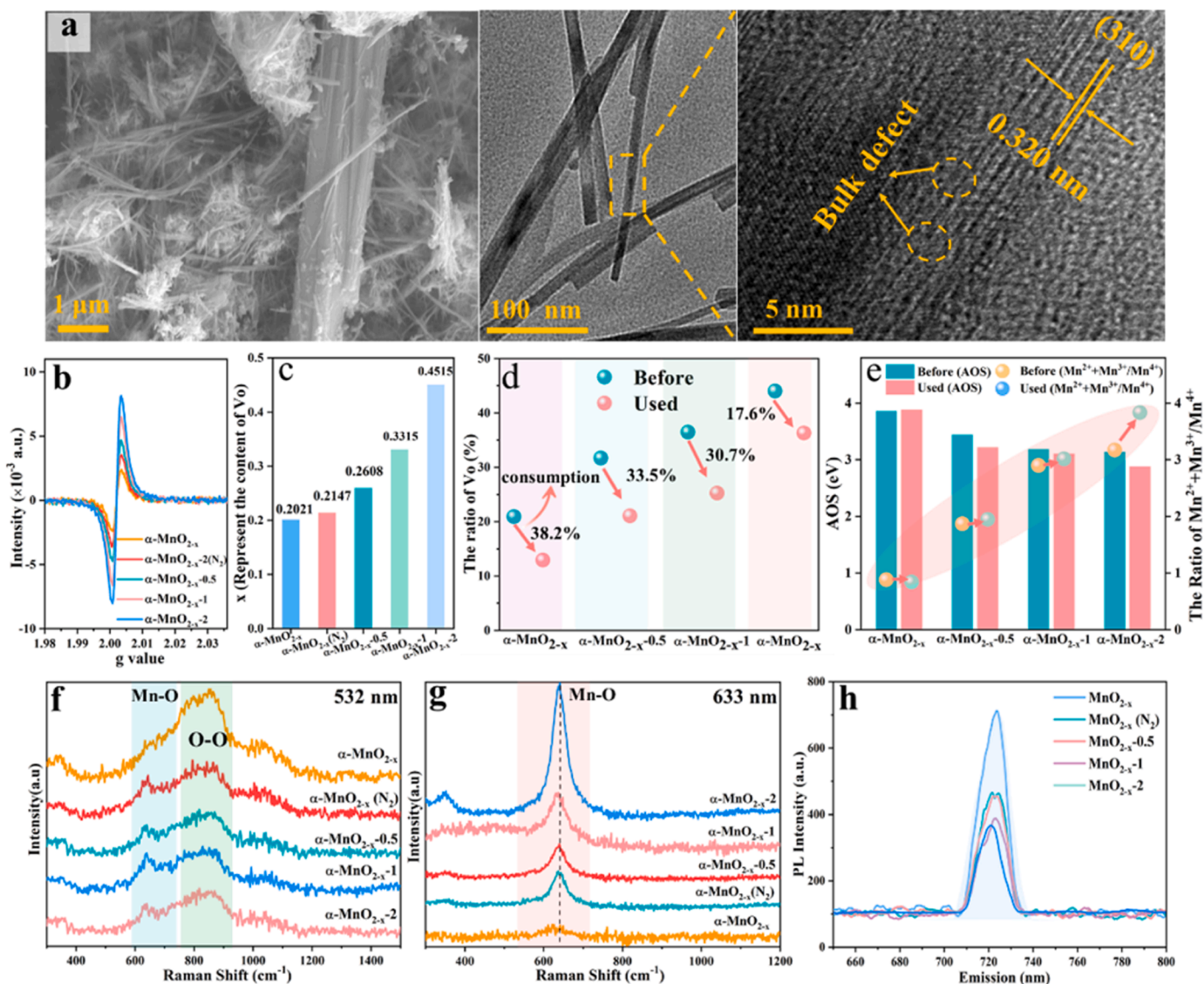


Fig. 1. SEM and HRTEM images of $\alpha\text{-MnO}_{2-x-2}$ (a); EPR signals assigned to Vo (b) and the Vo content determined by iodometric titration (c) of $\alpha\text{-MnO}_{2-x}$ samples; the changes of Vo content (d) and AOS and $(\text{Mn}^{2+}+\text{Mn}^{3+})/\text{Mn}^{4+}$ ratio (e) determined by XPS spectroscopy of synthesized catalysts before and after used; the Raman spectra.

with the wavelengths at 532 nm (f) and 633 nm (g), and PL spectra (h) of various catalysts.

release of O atom from the lattice and the formation of Vo sites. As determined by iodometric titration, the quantitative Vo content followed the order of $\alpha\text{-MnO}_{2-x}$ ($x = 0.2021$) < $\alpha\text{-MnO}_{2-x-2}(\text{N}_2)$ ($x = 0.2147$) < $\alpha\text{-MnO}_{2-x-0.5}$ ($x = 0.2608$) < $\alpha\text{-MnO}_{2-x-1}$ ($x = 0.3315$) < $\alpha\text{-MnO}_{2-x-2}$ ($x = 0.4515$) (Fig. 1c).

The detailed chemical state of Vo -modified $\alpha\text{-MnO}_{2-x}$ was investigated by several spectral characterizations. XPS spectrum revealed a shift in the binding energy of O 1s in calcinated $\alpha\text{-MnO}_{2-x}$ to a lower value (529.51 eV) compared to the pristine sample (529.98 eV) (Fig. S6a). This shift indicated that the electron transfer capacity of $\alpha\text{-MnO}_{2-x}$ was strengthened by Vo through weakening bonds between atoms to reduce binding ability of nucleus to the outer electrons [39]. In addition, three characteristic peaks were obviously observed in O 1s peaks, corresponding to lattice oxygen species (~ 529.65 eV), low-coordinated oxygen adsorbed in Vo (~ 531.34 eV, e.g., O^\cdot , O^{2-} and OH groups), and surface residual hydroxyl molecules (O_{surf}) (~ 532.64 eV) [27]. And the intensity proportion (Fig. 1d) of Vo indexed peaks raised from 31.7 % to 44.0 % as the calcination time increased from 0.5 to 2 h. The electrons occupying O 2p orbital became

delocalized with the formation of such large amount of Vo [40]. Therefore, the valences of neighboring Mn decreased to maintain charge balance, as indicated by the increased ratios of $(\text{Mn}^{3+}+\text{Mn}^{2+})/\text{Mn}^{4+}$ in Mn 2p deconvolution from 1.56 to 2.64 with extended calcination time (Fig. 1e and Fig. S6b). Correspondingly, the gradual decrement of average oxidation state (AOS) values with the increased proportion of Vo from $\alpha\text{-MnO}_{2-x}$ to $\alpha\text{-MnO}_{2-x-2}$ also verified the reduction of Mn (Fig. 1e and Fig. S6c). These results indicated that the formation of Vo was accompanied by the production of unsaturated metal centers, which would co-contribute to the enhancement of the catalytic performance of $\alpha\text{-MnO}_{2-x}$ samples.

It was worth mentioning that the content information of Vo in $\alpha\text{-MnO}_{2-x}$ samples observed from EPR, iodometric titration and XPS measurements was entirely different (Fig. 1b-d). This disparity was caused by the difference of these measurement techniques in the detection depth of catalyst structures. For instance, iodometric titration, based on chemical redox reactions, might only could detect surface or subsurface information of Vo . However, the detection depth of XPS up to 5 nm, which allowed it to approach the bulk of partial $\alpha\text{-MnO}_{2-x}$

samples with diameters as small as 10–20 nm. As for EPR, under the influence of an external strong magnetic field, could detect all unpaired electron signals trapped in both surface and bulk Vo. In other words, EPR techniques could comprehensively determine the Vo content on the surface and in the bulk of $\alpha\text{-MnO}_{2-x}$ samples. Thus, it could be concluded that Vo concentration varied within different depth ranges in $\alpha\text{-MnO}_{2-x}$ samples.

To further identifying the spatial position of Vo and its evolution, Raman spectroscopy analysis was conducted using two different excitation wavelengths at 532 nm and 633 nm (Fig. 1f–g). As shown in Fig. 1f, shifts at $\sim 640\text{ cm}^{-1}$ under the condition of short excitation wavelengths at 532 nm were attributed to the A_g spectral species resulting from the breathing vibrations of Mn–O in the $[\text{MnO}_6]$ octahedra in the tetragonal cryptomelane-type framework [41] [30]. These shifts were used to determine the Vo content in surface and subsurface of samples [42]. The peak intensity obviously increased after calcination under H_2 atmosphere (Table S1), suggesting the formation of more surface Vo in $\alpha\text{-MnO}_{2-x}$. Nevertheless, the intensity variation was insignificant with extended treatment time, indicating that surface Vo did not change. Vice versa, the Raman peak intensity at $\sim 830\text{ cm}^{-1}$, corresponding to the lattice oxygen species (O_2^-), decreased after calcination under H_2 treatment and remained relatively constant thereafter [41]. Moreover, the photoluminescence (PL) spectroscopy was conducted to identify the content of surface Vo by detecting improvements in the separation of photo-induced electrons and holes caused by surface Vo [31]. PL intensity change were negligible, inferring limited enhancement of electron transfer that mediated by surface Vo (Fig. 1h). These results collectively indicated that the content of surface Vo remained constant in calcinated $\alpha\text{-MnO}_{2-x}$. However, EPR, XPS and iodometric titration results showed that the concentration of Vo in $\alpha\text{-MnO}_{2-x}$ increased with the extension of annealing time. Similar results were also found in previous study [31], suggesting that the increased Vo concentration was attributed to the formation of bulk Vo

when the catalyst was calcined in a high H_2 concentration atmosphere. Hence, the bulk Vo information in $\alpha\text{-MnO}_{2-x}$ was examined using visible Raman spectroscopy at longer excitation wavelengths of 633 nm (Fig. 1g) [43]. As anticipated, an obvious peak at $\sim 640\text{ cm}^{-1}$ was observed in $\alpha\text{-MnO}_{2-x-2}$, verifying the formation of bulk Vo [32]. Compared with pristine $\alpha\text{-MnO}_{2-x}$, the peak intensity at $\sim 640\text{ cm}^{-1}$ in H_2 -treated $\alpha\text{-MnO}_{2-x}$ increased significantly with prolonged calcination time (Table S1), indicating an increase in bulk Vo content with long treatment time. Admittedly, longer calcination times would degrade crystallinity and destroy the original structure of $\alpha\text{-MnO}_2$, facilitating the generation of bulk Vo [37]. This same result was also obtained through UV-Visible near infrared diffuse-reflectance-spectroscopy (UV-vis-NIR DR), which characterized enhanced light absorption and reduced band gap in the visible and NIR regions due to the presence of bulk Vo [31] (Fig. S7a–c). The light absorption of $\alpha\text{-MnO}_{2-x}$ intensified with prolonged treatment time, confirming the increase of bulk Vo content from $\alpha\text{-MnO}_{2-x}$ to MnO_{2-x-2} .

Comprehensively, $\alpha\text{-MnO}_{2-x}$ with varying Vo concentration could be obtained through calcination under H_2 and N_2 atmosphere for 0–2 h. And Vo were categorized into surface Vo and bulk Vo according to their spatial positions within the catalyst. Specifically, comparable surface Vo formed initially and remained unchanged, while the concentration of bulk Vo kept increasing with the calcination time.

3.2. Enhanced performance of selective catalytic ozonation

The catalytic performance of as-prepared $\alpha\text{-MnO}_{2-x}$ was explored using ATZ as the target pollutant in O_3 system. Only $\sim 36\%$ of ATZ was removed in O_3 alone system within 10 min ($k_{\text{obs}} = 0.044\text{ min}^{-1}$) due to the limited reactivity ($k_{\text{O}_3/\text{ATZ}} = 6.0\text{ M}^{-1} \cdot \text{s}^{-1}$) [44] (Fig. S8a–b). While the removal of ATZ significantly increased from $\sim 41.6\%$ to $\sim 96.5\%$ with the addition of as-prepared $\alpha\text{-MnO}_{2-x}$ (Fig. 2a). Since single $\alpha\text{-MnO}_{2-x}$ exhibited negligible adsorption of ATZ ($\sim 2\%$ removal) (Fig. S8c), and

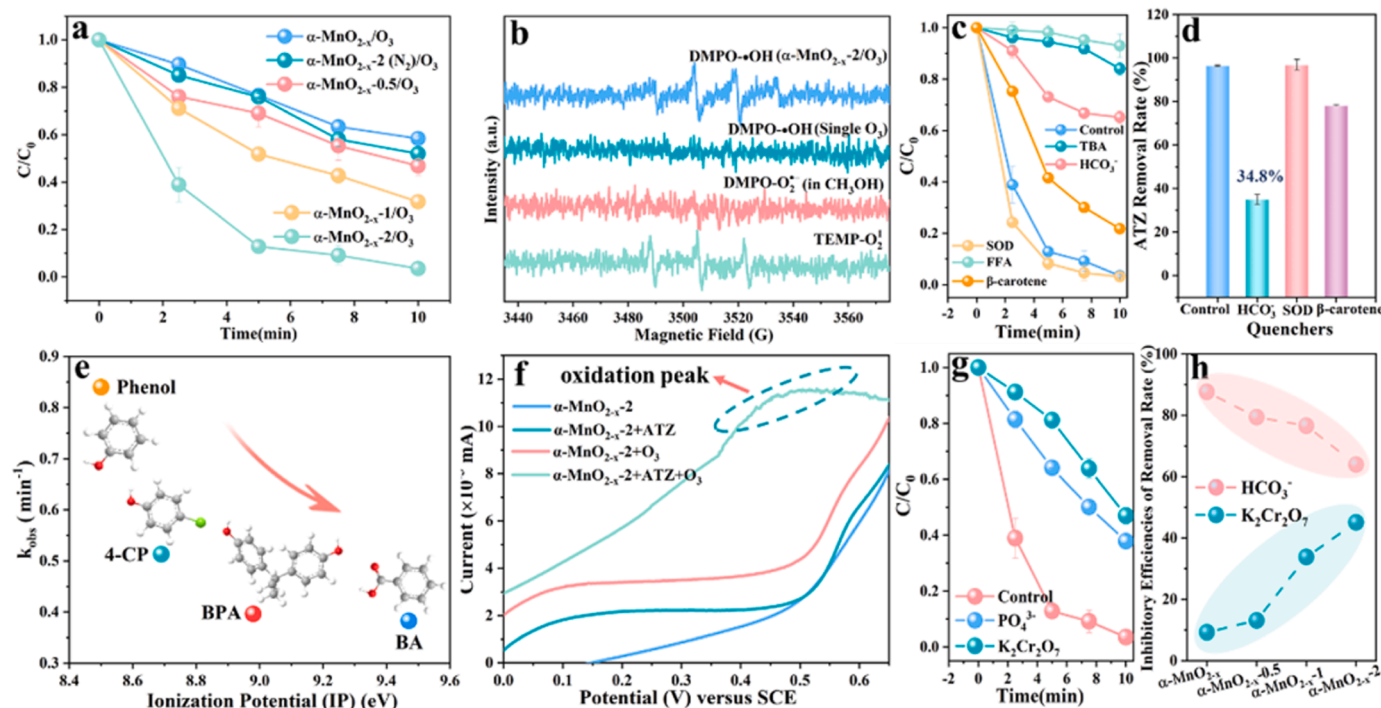


Fig. 2. The degradation curves of ATZ in a series of $\alpha\text{-MnO}_{2-x}/\text{O}_3$ systems (a); DMPO- $\text{SO}_4^{\cdot-}/\cdot\text{OH}/\text{O}_2^{\cdot-}$ and TEMP- $\text{O}_2^{\cdot-}$ signals observed in different solvents (b); the degradation curves (c) and removal rate (d) of ATZ under different quenching conditions; different organics degraded by $\alpha\text{-MnO}_{2-x-2}/\text{O}_3$ system (e); LSV obtained in the presence of different reactants (f); the degradation curves of ATZ under the effect of PO_4^{3-} and $\text{K}_2\text{Cr}_2\text{O}_7$ (g); the inhibitory efficiencies of the removal rates of ATZ under the effect of HCO_3^- and $\text{K}_2\text{Cr}_2\text{O}_7$ (h). ($[\text{O}_3] = 4\text{ mg/L}$, $[\alpha\text{-MnO}_{2-x}]_0 = 0.03\text{ g/L}$, $[\text{ATZ}]_0 = 2\text{ mg/L}$, $[\text{DMPO}]_0 = 100\text{ mM}$, $[\text{TEMP}]_0 = 100\text{ mM}$, $[\text{SOD}] = 100\text{ U/mL}$, $[\text{Quenchers}] = 10\text{ mM}$, $T = 25\text{ }^\circ\text{C}$ and $\text{pH}_0 = 7.0$).

the leached Mn ions (0.018 mg/L) from $\alpha\text{-MnO}_{2-x}/\text{O}_3$ system showed an insignificant catalytic effect on ozonation (Fig. S8d), the superior ATZ elimination was attributed to the excellent heterogeneous catalytic performance of $\alpha\text{-MnO}_{2-x}$. Compared to pristine $\alpha\text{-MnO}_{2-x}$, the reaction rate constant of ATZ was significantly improved about 5.8 times ($k_{\text{obs}}=0.057\text{--}0.33\text{ min}^{-1}$) in H_2 -treated $\alpha\text{-MnO}_{2-x-2}/\text{O}_3$ system (Fig. S9a), and the catalytic performance followed the order of $\alpha\text{-MnO}_{2-x} < \alpha\text{-MnO}_{2-x-2}(\text{N}_2) < \alpha\text{-MnO}_{2-x-0.5} < \alpha\text{-MnO}_{2-x-1} < \alpha\text{-MnO}_{2-x-2}$. Furthermore, compared with previous studies [18,45–49], $\alpha\text{-MnO}_{2-x-2}/\text{O}_3$ system required lower catalyst and O_3 demand and could achieve efficient ATZ removal in a shorter reaction time (Table S2). This highlighted the excellent catalytic performance of $\alpha\text{-MnO}_{2-x-2}$ in comparison to previously reported catalysts. Recall that the Vo content in $\alpha\text{-MnO}_{2-x}$ followed the same order as catalytic performance, it was reasonable to deduce that the Vo were the vital factor facilitating the activity of $\alpha\text{-MnO}_{2-x-2}$ in O_3 catalyzation [12,18,27,28].

To further decipher the enhanced decontaminant performance of $\alpha\text{-MnO}_{2-x}/\text{O}_3$, EPR spectroscopy using 5,5-dimethyl-1-pyrroline-noxide (DMPO) and 2,2,6,6-tetramethyl-4-piperidinol (TEMP) as the spin trapping agents was applied to determine the ROSs involved in the $\alpha\text{-MnO}_{2-x-2}/\text{O}_3$ process. EPR signals were negligible in single O_3 system (Fig. 2b), while distinct characteristic peaks of DMPO- $\bullet\text{OH}$ adducts (quartet with 1:2:2:1 signal intensity) were obtained with the addition of $\alpha\text{-MnO}_{2-x-2}$, indicating the formation of $\bullet\text{OH}$ derived from the O_3 catalyzation by $\alpha\text{-MnO}_{2-x-2}$. Also, typical ROS of $^1\text{O}_2$ was detected by the EPR signal of TEMPO- $^1\text{O}_2$ with relative intensities of 1:1:1. As for $\text{O}_2^{\bullet-}$, which was usually formed in catalytic ozonation, it could not be determined in this system. It was probably on account of that the $\text{O}_2^{\bullet-}$ concentration was too low to be traced. Radical scavenging experiments were further conducted to verify the contribution of $\bullet\text{OH}$, $^1\text{O}_2$ and $\text{O}_2^{\bullet-}$ in organics abatement. Notably, SOD ($k_{\text{SOD}/\text{O}_2^{\bullet-}} = 2.4 \times 10^9\text{ M}^{-1}\text{ s}^{-1}$) showed inappreciable influence on ATZ removal, confirming the negligible effect of $\text{O}_2^{\bullet-}$ (Fig. 2c) [50]. Since TBA ($\bullet\text{OH}$ scavenger) and furfuryl alcohol (FFA, $^1\text{O}_2$ scavenger) had significant influence on O_3 decomposition (Fig. S10), HCO_3^- and β -carotene were applied as scavengers instead to interpret the role of $\bullet\text{OH}$ and $^1\text{O}_2$ in ATZ abatement process, respectively. HCO_3^- ($k_{\text{OH}/\text{HCO}_3^-} = 8.5 \times 10^6\text{ M}^{-1}\text{ s}^{-1}$) showed a noticeable inhibitory effect ($\sim 61.7\%$) on ATZ removal (Fig. 2d), identifying that $\bullet\text{OH}$ played a critical role in ATZ degradation in the $\alpha\text{-MnO}_{2-x-2}/\text{O}_3$ system [18]. The removal of ATZ was inhibited $\sim 18.3\%$ with β -carotene, implying the minor contribution of $^1\text{O}_2$. In addition, the second-order rate constant of ATZ with $^1\text{O}_2$ was too low (lower than $4 \times 10^4\text{ M}^{-1}\text{ s}^{-1}$) to oxidize ATZ [7,51]. Therefore, $^1\text{O}_2$ was not responsible for ATZ degradation in $\alpha\text{-MnO}_{2-x-2}/\text{O}_3$ system. This phenomenon often appeared in Vo-induced AOPs, where the generation of $^1\text{O}_2$ didn't directly cause pollutant degradation but acted as intermediate species to promote electron recycling process around Vo in the presence of oxidants, and finally enhanced the organics abatement indirectly [21]. Above results suggested that $\bullet\text{OH}$ -dominated ROS pathway removed only a portion of ATZ in the $\alpha\text{-MnO}_{2-x-2}/\text{O}_3$ system. Apparently, additional decontamination processes were existed to completely remove the remaining ATZ. Such similar process has also been found in our previous studies and recent reports [18,52], possibly attributing to the nonnegligible contribution of non-radical pathways of ETP for organics abatement in catalytic ozonation.

Since the ETP has the typical characteristic of selectively degrading organics, four typical organic contaminants (i.e., phenol, chlorophenol (4-CP), bisphenol A (BPA) and benzoic acid (BA)) with similar reactivity to $\bullet\text{OH}$ ($k_{\text{phenol}/\bullet\text{OH}} = 6.6 \times 10^9\text{ M}^{-1}\text{ s}^{-1}$, $k_{4\text{-CP}/\bullet\text{OH}} = 7.6 \times 10^9\text{ M}^{-1}\text{ s}^{-1}$, $k_{\text{BPA}/\bullet\text{OH}} = 6.9 \times 10^9\text{ M}^{-1}\text{ s}^{-1}$, $k_{\text{BA}/\bullet\text{OH}} = 5.9 \times 10^9\text{ M}^{-1}\text{ s}^{-1}$) were treated in $\alpha\text{-MnO}_{2-x-2}/\text{O}_3$ system [44,53]. An interesting phenomenon was found: the removal efficiencies of these contaminants were not consistent with their reactivity to $\bullet\text{OH}$ (Fig. S11), revealing the selective characteristic of $\alpha\text{-MnO}_{2-x-2}/\text{O}_3$ system. Instead, the values of k_{obs} were negatively correlated with their ionization

potential (IP, phenol (8.50 eV) < 4-CP (8.69 eV) < BPA (8.98 eV) < BA (9.47 eV)) in $\alpha\text{-MnO}_{2-x-2}/\text{O}_3$ system (Fig. 2e), displaying the typical characteristic of ETP. Moreover, in situ linear sweep voltammetry (LSV) also provided the direct evidence of ETP [54] (Fig. 2f). With the introduction of O_3 , the current density increased obviously, which was different from the addition of ATZ, indicating the accelerated electron transfer from the electron-rich $\alpha\text{-MnO}_{2-x-2}$ surface to the electrophilic O_3 . Besides, a noticeable oxidation peak, along with a remarkable increase in current, was observed in the co-existence of O_3 and ATZ, suggesting the enhanced ETP in the reaction interface [54]. To further evaluate the contribution of ETP, $\text{K}_2\text{Cr}_2\text{O}_7$ ($E_{\text{h}}^0 = 1.33\text{ V}$), a commonly used single electron scavenger, was adopted to quench the ETP [55]. As expected, ATZ removal rate was suppressed by $\sim 44.0\%$ with the introduction of $\text{K}_2\text{Cr}_2\text{O}_7$ into $\alpha\text{-MnO}_{2-x-2}/\text{O}_3$ system (Fig. 2g), firmly confirming the significant role of ETP pathway in $\alpha\text{-MnO}_{2-x-2}/\text{O}_3$ system. Moreover, it was noteworthy that the contribution of ETP to ATZ abatement from pristine $\alpha\text{-MnO}_{2-x}/\text{O}_3$ to $\alpha\text{-MnO}_{2-x-2}/\text{O}_3$ systems was entirely distinct, specifically manifested as enhanced inhibitory efficiencies (9.23, 13.11, 33.84, 45.04 %) of the removal rates of ATZ with the introduction of $\text{K}_2\text{Cr}_2\text{O}_7$ in $\alpha\text{-MnO}_{2-x}/\text{O}_3$ systems (Fig. 2h and Fig. S12a). The detailed calculation process is shown in Text S7. These results were in accordance with the $\bullet\text{OH}$ quenching experiments that the inhibitory efficiencies of the removal rates of ATZ with HCO_3^- introduction decreased from 87.6 % in pristine $\alpha\text{-MnO}_{2-x}/\text{O}_3$ to 63.90 % in $\alpha\text{-MnO}_{2-x-2}/\text{O}_3$ systems (87.6, 79.38, 76.60, 63.90 %) (Fig. 2h and Fig. S13a). Notably, $\alpha\text{-MnO}_{2-x}/\text{O}_3$ systems embodied the impressive selective characteristic of O_3 decomposition to form ETP, ultimately inducing the selective degradation of organics. This phenomenon was firstly observed in Vo-involved metal-based catalytic ozonation process.

3.3. Identification of Vo as the active sites

To investigate the underlying factors that induced the selective catalyzation of O_3 by Vo-modified $\alpha\text{-MnO}_{2-x}$, potential active sites were systematically evaluated. As aforementioned, leached Mn ions had negligible catalytic effect on O_3 , indicating that the major catalyzation process occurred on the surface of $\alpha\text{-MnO}_{2-x}$. The active sites on catalyst surface commonly composed of typical Lewis acid sites (e.g., Vo and metal cations) and surface hydroxyl groups ($-\text{OH}$) connected to metal cations [18]. The single-bonded O atom in O_3 molecule preferred to bond with the Mn to form a weak Mn-O covalent bond, rather than interacting with surface hydroxyl groups. And a strong interaction between O_3 and Vo existed due to the imprinting effect [18]. As a result, the catalytic performance of O_3 in $-\text{OH}$ involved configurations was much inferior to that in configurations involving $\text{Mn}^{2+}/\text{Mn}^{3+}$ and Vo sites [18]. The negative relationship between the content of surface $-\text{OH}$ in five $\alpha\text{-MnO}_{2-x}$ samples and ATZ degradation results also verified this view (Fig. S14). Moreover, surface $-\text{OH}$ commonly contributed to the ROSs pathway in the O_3 catalyzation process, further suggesting that surface $-\text{OH}$ was not the dominant factor inducing the selective catalyzation of O_3 .

To determine the potential activity of Lewis acid sites, a strong Lewis base, PO_4^{3-} , was applied to hinder the interaction between Lewis acid sites and O_3 [18]. Obviously, the catalytic performance ($\sim 62\%$) of $\alpha\text{-MnO}_{2-x-2}$ was completely inhibited (Fig. 2g, $\sim 36\%$ for O_3 alone), indicating the decisive role of surface Lewis acid sites in O_3 catalyzation. Specifically, thiocyanate ions (SCN^-), which could coordinate with metal redox sites to shield the electron transfer behavior of $\alpha\text{-MnO}_{2-x-2}$, showed negligible effect on the performance of electrochemical hydrogen evolution reduction (HER) (Fig. 3a). It showed an apparent distinction in comparison to the drastic reduction of HER performance in $\alpha\text{-MnO}_{2-x}$, suggesting that the contribution to O_3 catalyzation via electron transfer resulting from Mn redox sites was decreased with the introduction of Vo [56]. Likewise, only a slight decrease in ATZ removal rate was achieved with the addition of 10 mM SCN^- in $\alpha\text{-MnO}_{2-x-2}/\text{O}_3$

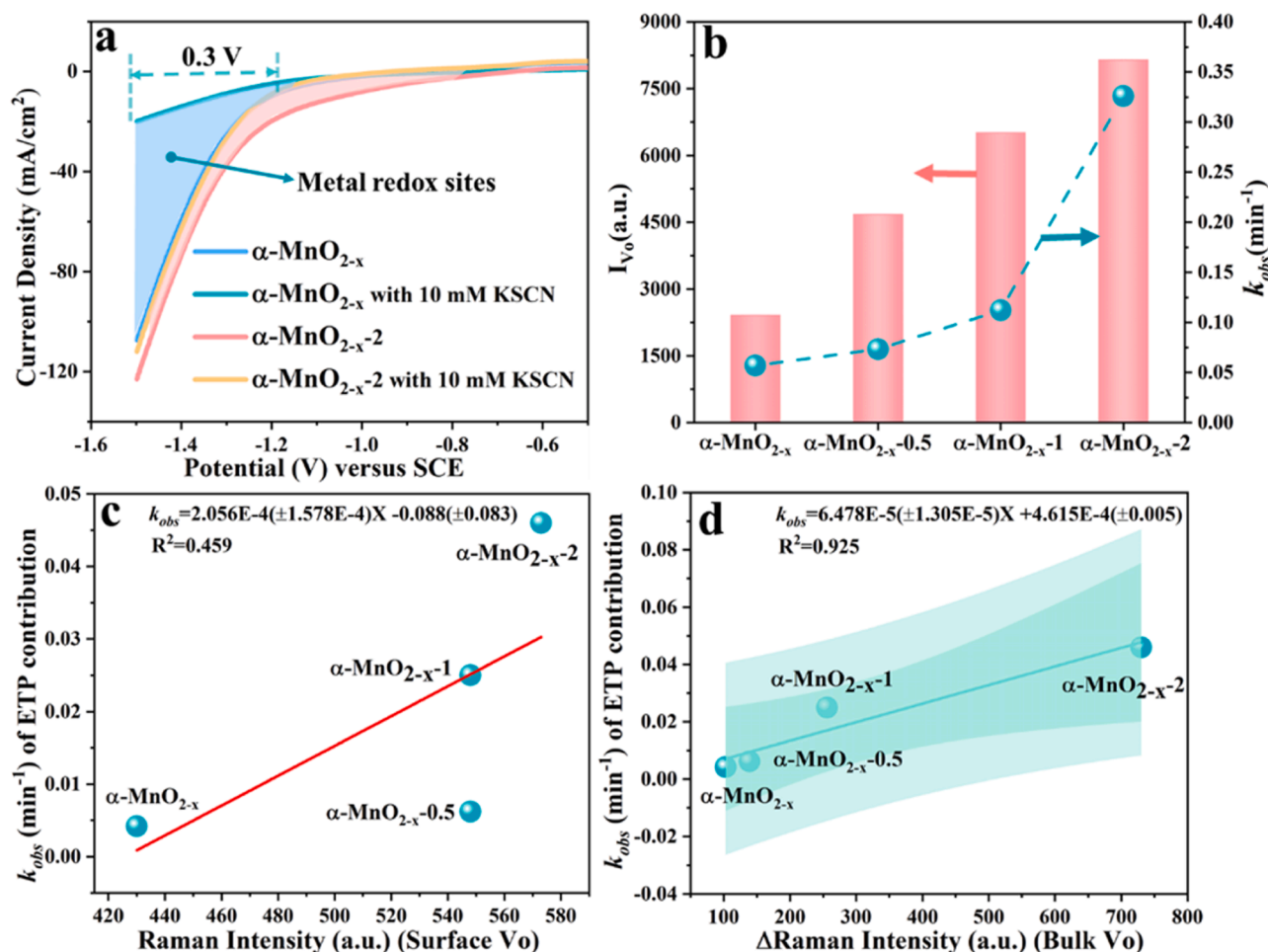


Fig. 3. The LSV HER curves of α -MnO_{2-x} and α -MnO_{2-x-2} with or without KSCN addition (0.2 M Na₂SO₄) (a); the changes of Vo content determined by EPR intensity (I_{Vo}) in α -MnO_{2-x} samples and k_{obs} calculated from different α -MnO_{2-x}/O₃ systems (b); the correlation between the surface Vo (c) or bulk Vo (d) determined from Raman spectra and k_{obs} of ETP contribution. ([O₃]=4 mg/L, [α -MnO_{2-x}]₀=0.03 g/L, [ATZ]₀=2 mg/L, T = 25 °C and pH₀ 7.0).

system, excluding the critical role of Mn redox sites for O₃ catalysis in Vo-modified metal-based catalyst (Fig. S15). In general, metal redox sites (Mn²⁺/Mn³⁺) acted as active sites for O₃ to form ion-exchange bridges to achieve electron transfer process and were responsible for ROSs production in catalytic ozonation processes [2,28,57,58]. However, the introduction of Vo adjacent to Mn redox sites would regulate the electrons configuration of the Mn 2p orbital to make the electrons confined around Vo. Since O₃ catalysis preferred to occur at the sites with higher electron density of Vo, the redox process of Mn sites was mainly regulated by Vo for keeping electron balance [27]. Therefore, it was reasonable to deduce that Vo dominated O₃ catalysis in Vo-modified α -MnO_{2-x}/O₃ systems.

The influence of Vo intensity (I_{Vo} , 2413.1 (α -MnO_{2-x}), 4674.7 (α -MnO_{2-x-0.5}), 6511.5 (α -MnO_{2-x-1}), 8144.4 (α -MnO_{2-x-2})) in α -MnO_{2-x} samples on the k_{obs} of ATZ degradation was investigated to confirm the role of Vo. More Vo corresponded larger k_{obs} , and obvious positive relationships were showed between k_{obs} and I_{Vo} of as-prepared α -MnO_{2-x} samples, verifying the significant role of Vo in improving the catalytic activity of α -MnO_{2-x} (Fig. 3b). Combined these results with the electron scavenging experiments mentioned above (Fig. 2g), it became evident that ETP emerged as the nonnegligible pathway in α -MnO_{2-x}/O₃ process. This was a typical feature of Vo-induced catalytic processes rather than metal redox sites, proving that Vo were the dominant active sites for O₃ catalysis to promote ATZ removal in Vo-modified α -MnO_{2-x}/O₃ systems. The particular effect of pH on the catalytic performance also confirmed that it was a Vo-triggered catalytic

process (Fig. S16, with detailed analysis in Text S10). Unexpectedly, the coefficient of determination (R^2) between I_{Vo} and k_{obs} gradually decreased from 0.934 to 0.644 (Fig. S9b-d) with the increase of Vo content from α -MnO_{2-x} to α -MnO_{2-x-2}. It indicated that the reaction kinetics process changed with the increase of Vo content in α -MnO_{2-x}/O₃ system. Also, it was noted in scavenging experiments results (Fig. 2h) that the O₃ catalyzed by Vo-modified α -MnO_{2-x} could induce both ETP and ROSs pathways simultaneously. And the contribution of these two pathways changed with the evolution of Vo (Fig. S13d, with detailed calculation processes shown in Text S11). Therefore, it was reasonable to deduce that the thermodynamic feature (ROSs or ETP) alteration was induced by Vo content and subsequently caused the difference in the kinetic behavior (k_{obs}) in Vo-modified α -MnO_{2-x}/O₃ systems. More specifically, the change in Vo content in α -MnO_{2-x} was mainly derived from the increase of bulk Vo with prolonged treatment time (Fig. 1f-g). That is, the introduction of bulk Vo shifted the thermodynamic feature from ROSs to ETP. On the other hand, the effect of surface Vo and bulk Vo was absolute different, leading to selective O₃ catalysis. To identify the definite function of Vo located at different spatial positions, a variety of structure-activity relationships in α -MnO_{2-x-2}/O₃ system were systematically investigated. Firstly, the k_{obs} of ETP pathway in different α -MnO_{2-x}/O₃ systems was calculated (detailed calculation processes are shown in Text S12). As anticipated, different from the poor relationship ($R^2 = 0.459$) between the k_{obs} of ETP pathway and surface Vo content (Fig. 3c), a good liner relationship ($R^2 = 0.925$) between the k_{obs} of ETP pathway and bulk Vo content was observed (Fig. 3d).

Apparently, the evolution of Vo from surface to bulk phase was the root cause of selective O₃ catalyzation, and converted ROSs to ETP pathways in α -MnO_{2-x}-2/O₃ systems. This unfamiliar phenomenon involving the modulation of different pathways relying on distinct Vo has never been reported.

3.4. Mechanism of Vo for inducing selective catalytic ozonation process

Based on the aforementioned experiment results and in-depth analysis, surface Vo determined the production of ROSs, while bulk Vo contributed to ETP pathway in α -MnO_{2-x}-2/O₃ systems. The question that remained was why this interesting phenomenon occurred? To answer this question, we further explored the underlying mechanism of Vo in inducing the selective catalytic ozonation process. As is known, ROSs evolution includes of two key steps: O₃ adsorption and catalyzation on α -MnO_{2-x} surface [27,32]. In this context, Vo tended to capture relatively unrestricted O atoms from its surroundings (e.g., O₂ and O₃) [27,29]. Especially, surface Vo approaching the solid-liquid-gas interface functioned as the preferential adsorption sites for O₃, achieving synchronous enhancement of adsorption and subsequent catalytic efficiency [26,27]. As displayed in Fig. 4a, in situ Raman spectra (532 nm) showed that the characteristic peaks of O-O vibration amplitude belonging to O₃ at 812 and 844 cm⁻¹ shifted to 786 and 877 cm⁻¹ in α -MnO_{2-x}-2/O₃ system, confirming the special bridging adsorption of O₃ onto the active sites on α -MnO_{2-x}-2 surface [59] (Eq. (1)). Moreover, this adsorption process mainly occurred around surface Vo sites, as evidenced by the first-principles computation results based on DFT. DFT calculation results showed that the α -MnO_{2-x}-2 exhibited lower

adsorption energy (-2.97 eV) and longer O-O bond length (1.46 Å) toward adsorbed O₃ than those of α -MnO_{2-x} (-2.19 eV and 1.39 Å) at surface Vo sites (Fig. 4d). Subsequently, the surface Vo could endow the adsorbed oxygen species with higher mobility and activity, as evidenced by lower desorption temperature (358 °C vs. 373 °C) and a higher peak intensity of α -MnO_{2-x}-2 compared to α -MnO_{2-x} in O₂-temperature programmed desorption (O₂-TPD) curve (Fig. S17) [60]. This unique adsorption effect of surface Vo on O₃ greatly accelerated the electron transfer process involved in O₃ decomposition, ultimately boosting the production and release of ROSs (Eqs. (2)–(5)) [27,29]. Generally, due to the formation of electron-rich fields within the micro area around Vo by the electron redistribution, the electrophilic O₃ preferred to approach and withdraw electrons from the surface Vo. The in situ Raman spectra (Fig. 4a) clearly displayed that the O₃ anchored at α -MnO_{2-x}-2 surface could accept the delocalized electrons from Vo to be dissociated into -O²⁻/O₂⁻ (Eq. (2)) and then reacted with another O₃ molecular to form -O₂²⁻ (Eq. (3)), resulting in the generation of new intermediate oxygen species, including peroxide species (-O₂²⁻, 877 cm⁻¹) [18] and atomic oxygen species (-O²⁻, 578 cm⁻¹) [18] in MnO_{2-x}-2/O₃. The peak intensity of the produced oxygen species gradually weakened as the reaction progressed (1–10 min) (Fig. 4b), indicating that these active oxygen species (-O²⁻, -O₂²⁻, and O₂^{*}) containing abundant free electrons easily reacted with the H₂O molecular or O₃ in aqueous solution, leading to protonation and transformation into •OH (Eqs. (4)–(5)). Whereas similar changes were not observed in α -MnO_{2-x} with limited surface Vo after reacting with O₃ (Fig. 4c), further verifying the impressive effect of surface Vo in facilitating the electron transfer from MnO_{2-x}-2 to O₃ for

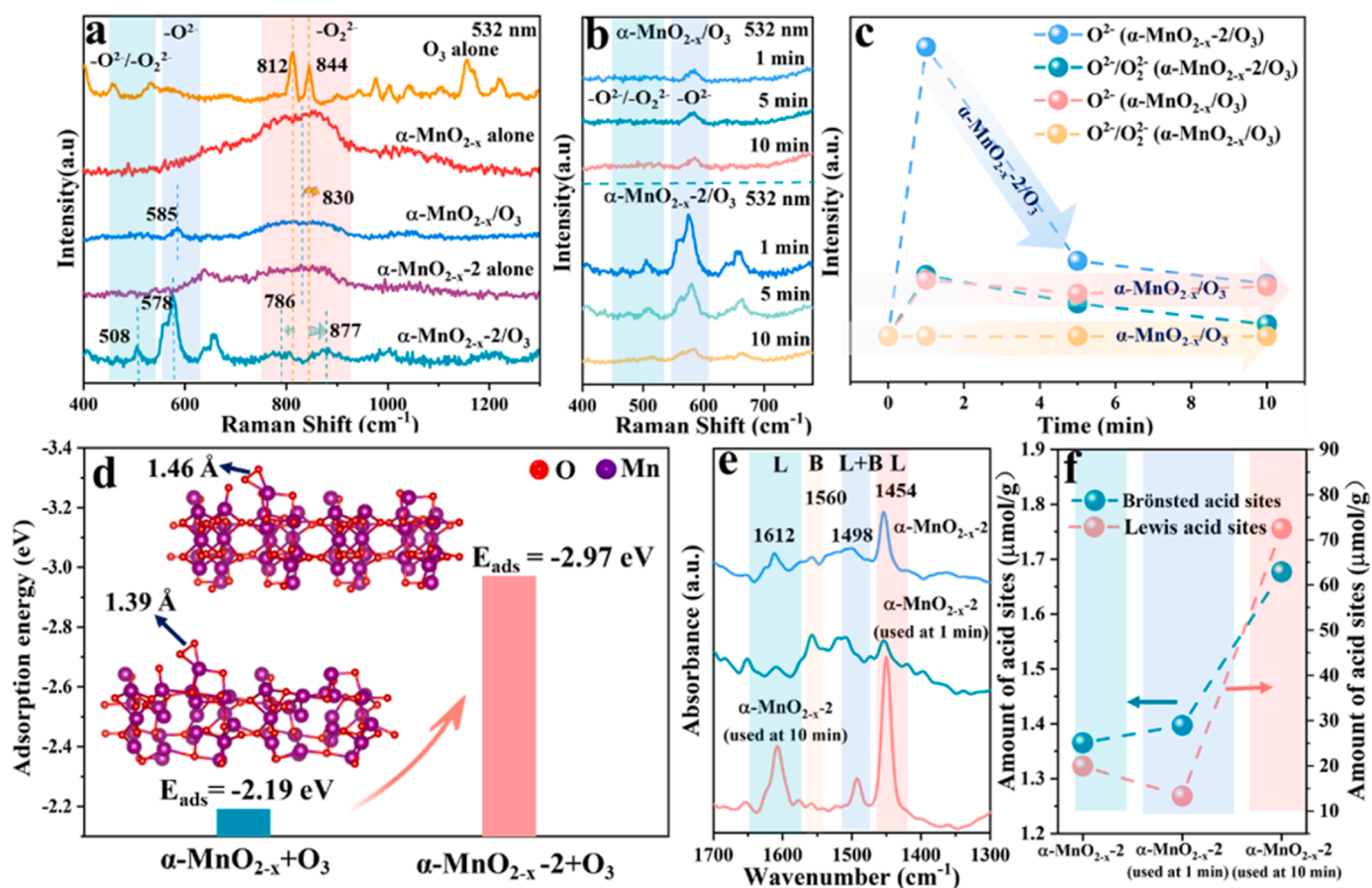
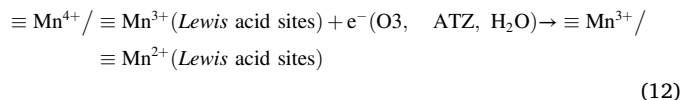
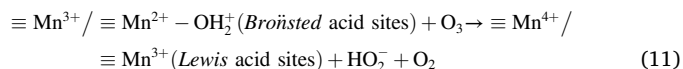
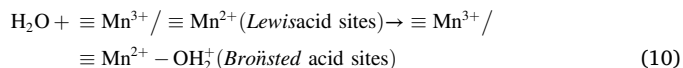
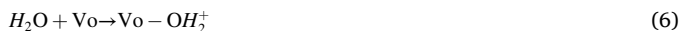
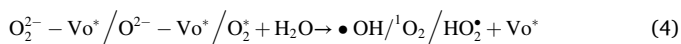
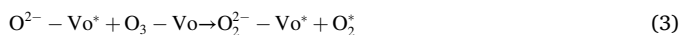
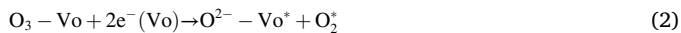


Fig. 4. In situ Raman spectra (532 nm) of O₃, α -MnO_{2-x}, α -MnO_{2-x}-2 and the reaction between them (a); the change of in situ Raman spectra (b) and oxygen species (c) in α -MnO_{2-x}/O₃ and α -MnO_{2-x}-2/O₃ systems as the reaction progressed (1–10 min); the adsorption energy of O₃ on α -MnO_{2-x} and α -MnO_{2-x}-2 (d); the infrared spectra of adsorbed pyridine (e) and the amount change of acid sites (f) in α -MnO_{2-x}-2 before and after reaction (degassing at 250 °C; L: Lewis acid sites, B: Brønsted acid sites). ([O₃]=4 mg/L, [α -MnO_{2-x}]₀=0.03 g/L, [ATZ]₀=2 mg/L, T = 25 °C and pH₀ 7.0).

•OH production.

As reported, surface Vo, as unsaturated electron centers, could not only promote direct electron transfer between O₃ and MnO_{2-x}-2 but also complexed with H₂O and mediated the neighboring metal redox sites to form new active intermediates to boost O₃ catalyzation [37]. In this way, the electron loss at the surface Vo could be compensated during these processes, which explained the unexpected increase in the (Mn²⁺+Mn³⁺)/Mn⁴⁺ ratio and the reduction of AOS value that occurred after reactions in α-MnO_{2-x}/O₃ system (Fig. 1e and Fig. S18a-b). In addition, the new active sites, surface-OH₂⁺, were generated through the adsorption of H₂O on Vo sites (Eq. (6)) under the strong electron-induced effect caused by surface Vo, as confirmed by the enhanced adsorption energy of H₂O on α-MnO_{2-x}-2 (-0.84 eV) in comparison to α-MnO_{2-x} (-0.55 eV) (Fig. S19a). Surface-OH₂⁺, trapped by surface Vo, tended to react with O₃ under the effect of electrostatic forces and hydrogen bonding to provide HO₃[•] and surface -OH (Eq. (7)) [37], which would further participate in O₃ catalyzation to produce •OH ultimately (Eqs. (8)–(9)). It was the key reason that Vo-modified catalysts possessed superior catalytic performance for O₃ in aquatic environment.

Besides, surface Vo re-localized the electron configuration of the adjacent metal cations exposed on the catalyst surface, contributing to the enrichment of unsaturated valence bonds (i.e., hanging bonds) belonging to metal redox sites outward [61]. It further endowed the metal redox sites near surface Vo with larger surface energy, causing them to react with H₂O and form more Brønsted acid sites by Eq. (10) [12]. This was confirmed by the increased peak intensity at 1560 and 1498 cm⁻¹ assigned to the pyridine adsorbed on Brønsted acid sites observed from Pyridine-FTIR spectra (Fig. 4e) [18]. Then, the Brønsted acid sites were consumed by O₃ to produce HO₂⁻ and further formed •OH and O₂^{•-} based on Eqs. (9)–(11) [12]. The consumed Brønsted acid sites were transformed into Lewis acid sites, which possessed unpaired electrons to act as electron shuttles and draw electrons from surrounding reactants (e.g., O₃, ATZ, H₂O) (Eq. (12)), promoting Brønsted acid sites regeneration (Eqs. (10)–(12)) (Fig. 1e and Fig. S18a-b) [12]. Pyridine-FTIR results could confirm these processes by showing a continuous increase in Brønsted acid sites with prolonged reaction time (Fig. 4f, Text S3, and Table S4). On this basis, surface Vo, with high electron density exposed onto the catalyst-solution interface, accelerated the electron transfer cycle between O₃ and α-MnO_{2-x}-2, which was generally recognized as the root for •OH production in α-MnO_{2-x}-2/O₃ systems [21,22,27,60]. As a result, surface Vo could not only donate delocalized electrons for direct O₃ catalyzation but also coordinated with H₂O molecular and mediated adjacent metal redox sites to form regenerated active sites, facilitating the production of •OH in catalytic ozonation.



Compared with surface Vo, bulk Vo exhibited completely different feature (e.g., thermodynamics and kinetics) in catalytic process because it could not directly interact with the substrates due to its long distance from the reaction interface. We conducted further investigations to provide an intuitive demonstration of the different electron transfer behavior in O₃ catalyzation induced by surface Vo and bulk Vo. Fig. S20a showed that the electron donating capacity (EDC) derived from mediated electrochemical oxidation (MEO) gradually increased from α-MnO_{2-x} to α-MnO_{2-x}-2 (Text S13), revealing that the electron donation capacity was enhanced with the constant enrichment of bulk Vo within α-MnO_{2-x} samples [62]. Moreover, the formation of bulk Vo within the interior of α-MnO_{2-x}-2 promoted the outflow of electrons inside catalyst to reaction interface to facilitate subsequent O₃ catalyzation, as confirmed by the smallest arc radius in electrochemical impedance spectroscopy (EIS) Nyquist plots (Fig. S20b) [39]. The theoretical computations based on the evolution of electron cloud after the introduction of bulk Vo further revealed this process at the atomic orbital level (Fig. 5a). Specifically, the charge density of Mn sites was weakened and drew the electron cloud around Vo, indicating that the presence of Vo in α-MnO_{2-x}-2 caused electrons to delocalize from Mn 2p orbitals and to be confined around Vo, forming constant electron-rich fields [20,21]. In this way, a continuous electron energy level was generated, inducing the release of electrons from the bulk of α-MnO_{2-x}-2 to its surface [32]. Subsequently, these escaped electrons participated in the similar above-mentioned catalytic ozonation process that dominated by surface Vo through electron transfer for •OH production. The deduction was further corroborated by the new in situ Raman peak at 508 cm⁻¹ corresponding to oxygen species (e.g., -O²⁻ and -O₂²⁻), which was decomposed from O₃ in α-MnO_{2-x}-2/O₃ system (Fig. 4a) [18].

As above mentioned, the electron consumption on surface Vo could be compensated to keep electron balance by complexing with H₂O molecular and mediating the adjacent metal sites to achieve rapid redox cycles. Accordingly, surface Vo dominated the enhancement of the •OH pathway for organics removal. However, bulk Vo, situated far from the reaction interface, needed to overcome a strong electron transition energy barrier to interact with H₂O molecular or newly formed active intermediates (e.g., Brønsted acid sites). Thus, after the bulk electrons were discharged to the surface, the electron compensation process possessed by surface Vo was not accessible to bulk Vo, resulting in an imbalance of the electron configuration in α-MnO_{2-x}-2. It was verified by the weakened charge density in α-MnO_{2-x}-2 and the enrichment of electrons around O atoms of O₃ after the participation of O₃ (Fig. 5d). In this way, bulk Vo transformed into an electron-deficient state (Vo^{*}). This electronic imbalance state would lead to the formation of an electronic relaxation phenomenon to attract the outside electrons [21]. Compared with H₂O molecular, ATZ and its degradation intermediates from •OH oxidation process contained more electron-donating groups (e.g., -NHR₂, -NH₂, -OH and -OR, Table S5), which preferred to donate electrons to the electron-deficient catalysts [21]. As a result, the electrons were transferred directly from organics to α-MnO_{2-x}-2, inducing ETP pathway to degrade and mineralize ATZ (Eq. (13)). Similar phenomena have also been observed in PMS systems [21]. The disparity in the chemical state of catalysts also verified the ETP process induced by bulk Vo. As shown in Fig. 1e and Fig. S18a-b, the observation of both slightly

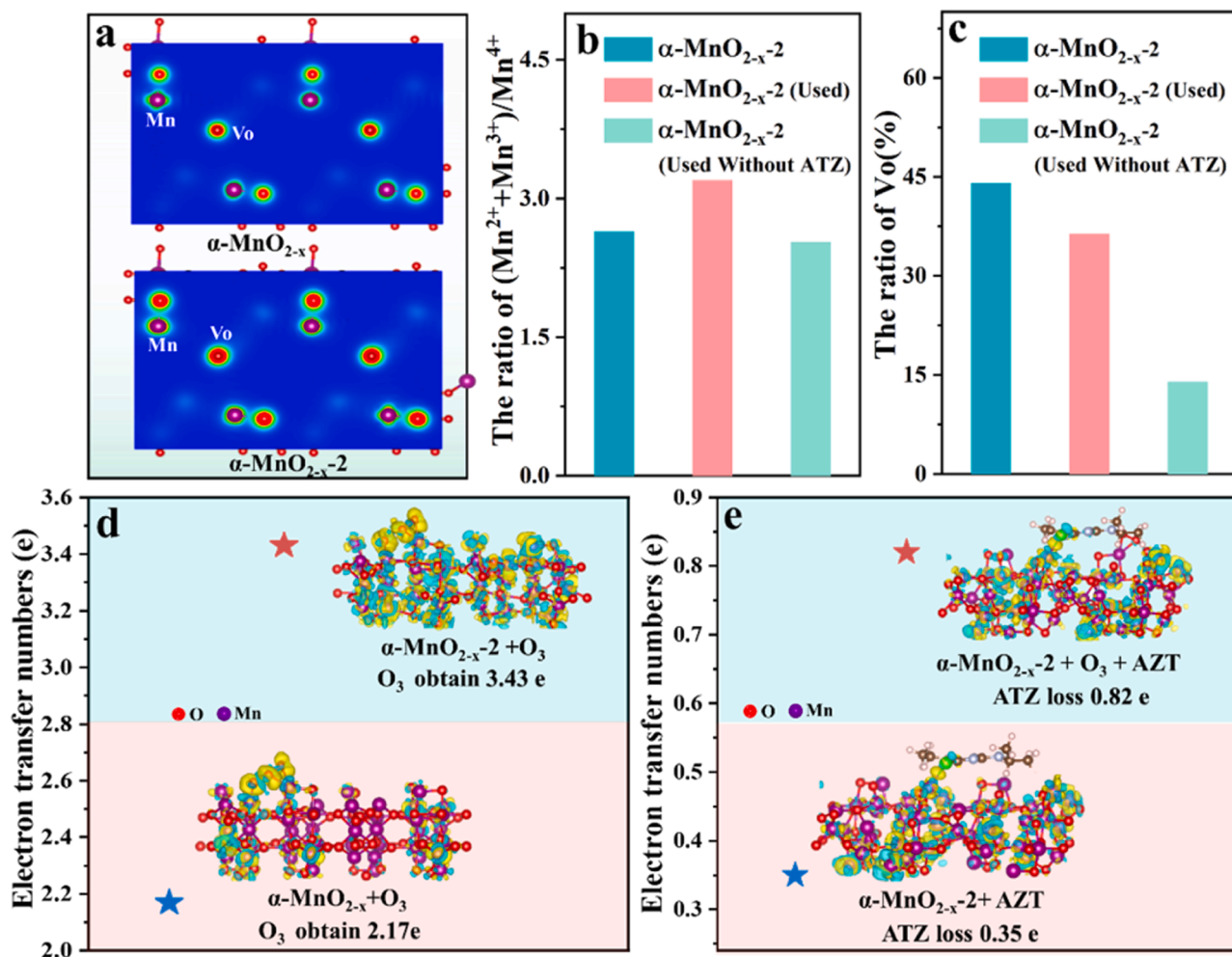
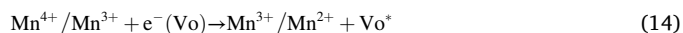
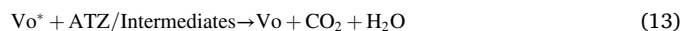


Fig. 5. The charge density of $\alpha\text{-MnO}_{2-x}$ and $\alpha\text{-MnO}_{2-x-2}$ (a); the change of the ratio of $(\text{Mn}^{2+} + \text{Mn}^{3+})/\text{Mn}^{4+}$ (b) and Vo (c) before and after used with or without ATZ; the charge transfer between O_3 and $\alpha\text{-MnO}_{2-x}$ or $\alpha\text{-MnO}_{2-x-2}$ (d); the charge transfer between ATZ and $\alpha\text{-MnO}_{2-x-2}$ with or without O_3 participation (e). The light green and light yellow denote the electron accumulation and electron depletion, respectively. ($[\text{O}_3] = 4 \text{ mg/L}$, $[\alpha\text{-MnO}_{2-x}]_0 = 0.03 \text{ g/L}$, $[\text{ATZ}]_0 = 2 \text{ mg/L}$, $T = 25^\circ\text{C}$ and $\text{pH}_0 7.0$).

reduction of Mn^{4+} or Mn^{3+} to Mn^{2+} or Mn^{3+} as well as the decreased AOS calculation results for the used $\alpha\text{-MnO}_{2-x-2}$ could be attributed to the electrons enrichment in Vo from ATZ, which reduced the adjacent Mn redox sites (Eq. (14)). This reduction process did not happen in the used $\alpha\text{-MnO}_{2-x-2}$ that derived from the $\alpha\text{-MnO}_{2-x-2}/\text{O}_3$ system without the addition of ATZ (Fig. 5b and Fig. S21), verifying that the ATZ indeed acted as electron donor for $\alpha\text{-MnO}_{2-x-2}$ in electron-deficient state. Also, the less consumption of Vo after catalyzation with the ATZ addition confirmed the electron compensation process (Fig. 5c). Furthermore, theoretical calculations were applied to determine the electron transfer between ATZ and MnO_{2-x-2} with and without O_3 participation. As shown in Fig. 5e, the charge transfer (0.82 e) between $\alpha\text{-MnO}_{2-x-2}$ and ATZ in the presence of O_3 was higher than that in the absence of O_3 (0.35 e). This confirmed that O_3 initially withdrew the electrons confined in the Vo sites of $\alpha\text{-MnO}_{2-x-2}$, and then ATZ served as an electron source to supplement electrons for $\alpha\text{-MnO}_{2-x-2}$, resulting in an impressive electron cycle and achieving ATZ degradation in ETP pathway. The stoichiometry efficiency of O_3 might be remarkably promoted by this efficient electron cycle. In order to confirm this conclusion, O_3 decomposition experiments were conducted in different $\alpha\text{-MnO}_{2-x}/\text{O}_3$ systems by setting the initial O_3 concentration at 4 mg/L (Text S7, Fig. S22a-b). Based on the ATZ removal and O_3 decomposition results, the specific oxidant efficiency (SOE) at 10 min of the reaction was calculated to evaluate the stoichiometry efficiency of O_3 (Text S7). As shown in

Fig. S22c, the SOE gradually increased from $\alpha\text{-MnO}_{2-x}/\text{O}_3$ system to $\alpha\text{-MnO}_{2-x-2}/\text{O}_3$ system (0.091, 0.16, 0.21, 0.37). This result confirmed the significant improvement in the stoichiometry efficiency of O_3 for ATZ removal in $\alpha\text{-MnO}_{2-x-2}/\text{O}_3$ system with an efficient electron cycle.



Based on results and discussions above, a novel selective O_3 catalyzation process modulated by surface and bulk Vo over $\alpha\text{-MnO}_{2-x}$ for ATZ degradation was observed and the underlying regulation mechanism was proposed. Firstly, the surface Vo in $\alpha\text{-MnO}_{2-x-2}$, endowed with abundant electrons in the micro area (Fig. 5a), had strong O_3 adsorption capacity (Eq. (1)), subsequently catalyzing O_3 into $\bullet\text{OH}$ through direct electron transfer (Eqs. (2)–(5)). Meanwhile, to remain electron balance, surface Vo tended to coordinate with H_2O to form $\text{Vo}-\text{OH}_2^+$ (Eq. (6)) and mediate the adjacent $\equiv\text{Mn}^{2+}/\equiv\text{Mn}^{3+}$ redox sites reacting with H_2O to form Brønsted acid sites (Eq. (10)), co-contributing to O_3 dissociation for $\bullet\text{OH}$ production (Eqs. (6)–(11)). Compared with surface Vo, bulk Vo showed completely different catalyzation features (e.g., kinetics and thermodynamics). On the one hand, bulk Vo, serving as electron-rich centers, mediated the direct electron transfer from bulk to surface and participated in O_3 catalyzation to form $\bullet\text{OH}$ for ATZ removal, even though they were located within the internal structure of $\alpha\text{-MnO}_{2-x}$. On

the other hand, the direct electron compensation process was inaccessible for bulk Vo, which tended to withdraw the electrons from both ATZ and its intermediates through ETP pathway to sustain the electrostatic balance (Eq. (13), Fig. 5e). Therefore, with the synergistic effect of •OH and ETP, which possessed both strong oxidation capacity and selectivity, α -MnO_{2-x}/O₃ system offered unique advantages, including: 1) improved TOC removal rate (~38 % vs ~20 %) and less accumulation of macromolecular intermediates compared with the α -MnO_{2-x}/O₃ system (Figs. S23–25, with detailed analysis in Text S14); 2) exceptional interference elimination capacity in practical water (Figs. S26, with detailed analysis in Text S15); 3) stable catalytic activity with 85 % ATZ removal after five consecutive cycles (Fig. S27).

4. Conclusions

For the first time, this study demonstrated that Vo at different spatial positions of metal-based catalysts induced entirely different regulation behaviors in O₃ catalyzation to boost the ROSs and ETP pathway for organics removal. Benefitting from their strong affinity with oxygen species and excellent performance to enhance electrons transfer, Vo were identified as dominant active sites in α -MnO_{2-x}/O₃ process. The evolution of Vo from surface to bulk resulted in the selective O₃ catalyzation and converted ROSs to ETP pathways in catalytic ozonation. Specifically, surface Vo functioned as preferential adsorption sites for O₃, achieving synchronous enhancement of adsorption and subsequent ROSs production. Besides, surface Vo also coordinated with H₂O molecular and mediated the adjacent metal redox sites to form regenerated active sites, facilitating the production of •OH. As for bulk Vo, on the one hand, they induced the release of electrons from the bulk of α -MnO_{2-x} to its surface, participating in the similar catalytic ozonation process dominated by surface Vo. On the other hand, bulk Vo tended to withdraw the electrons from organics to sustain electrostatic balance, creating ETP pathway for organics removal. Remarkably, this unique ROSs and ETP collaboration system with strong oxidation and selectivity was beneficial to achieve efficient removal and mineralization of refractory organics in a complex practical background.

CRediT authorship contribution statement

Liyang Wu: Investigation, Data curation, Writing – original draft. **Zonglin Wang:** Data curation. **Jiaye Liu:** Investigation. **Caihong Liu:** Writing – review & editing. **Xueyan Li:** Conceptualization, Supervision. **Yixuan Zhang:** Data curation. **Wei Wang:** Curation. **Jun Ma:** Supervision, Validation. **Zhiqiang Sun:** Funding supporting, Editing.

Declaration of Competing Interest

The authors declare that they have no known competing financial interests or personal relationships that could have appeared to influence the work reported in this paper.

Data availability

Data will be made available on request.

Acknowledgements

The support from National Natural Science Foundation of China (Grant No. 52000050), Postdoctoral Science Foundation of China (Grant No. 2020M670913), Heilongjiang Postdoctoral Fund (Grant No. LBH-Z20063) and State Key Laboratory of Urban Water Resource and Environment (Harbin Institute of Technology) (Grant No. 2021TS22) are greatly appreciated.

Appendix A. Supporting information

Supplementary data associated with this article can be found in the online version at doi:10.1016/j.apcatb.2023.123526.

References

- [1] S. Afzal, X. Quan, J. Zhang, High surface area mesoporous nanocast LaMO₃ (M=Mn, Fe) perovskites for efficient catalytic ozonation and an insight into probable catalytic mechanism, *Appl. Catal. B Environ.* 206 (2017) 692–703.
- [2] J. Bing, C. Hu, Y. Nie, M. Yang, J. Qu, Mechanism of catalytic ozonation in Fe₂O₃/Al₂O₃@SBA-15 aqueous suspension for destruction of ibuprofen, *Environ. Sci. Technol.* 49 (2015) 1690–1697.
- [3] G. Yu, Y. Wang, H. Cao, H. Zhao, Y. Xie, Reactive oxygen species and catalytic active sites in heterogeneous catalytic ozonation for water purification, *Environ. Sci. Technol.* 54 (2020) 5931–5946.
- [4] A. Xu, S. Fan, T. Meng, R. Zhang, Y. Zhang, S. Pan, Y. Zhang, Catalytic ozonation with biogenic Fe-Mn-Co oxides: biosynthesis protocol and catalytic performance, *Appl. Catal. B Environ.* 318 (2022), 121833.
- [5] J. Liang, K. Chen, X. Duan, L. Zhao, H. Qiu, X. Xu, X. Cao, pH-dependent generation of radical and nonradical species for sulfamethoxazole degradation in different carbon/persulfate systems, *Water Res.* 224 (2022), 119113.
- [6] J. Xie, Y. Zheng, Q. Zhang, S. Li, J. Gu, M. Zhou, C. Wang, Y. Li, Constructing a carbon sphere-embedded Fe⁰ for accelerating electro-peroxone oxidation effectively: the dual catalytic role with O₃ and H₂O₂, *Appl. Catal. B Environ.* 320 (2023), 121935.
- [7] J. Lee, U. von Gunten, J.H. Kim, Persulfate-based advanced oxidation: critical assessment of opportunities and roadblocks, *Environ. Sci. Technol.* 54 (2020) 3064–3081.
- [8] Z.Y. Dong, Q. Zhang, B.Y. Chen, J.M. Hong, Oxidation of bisphenol A by persulfate via Fe₃O₄- α -MnO₂ nanoflower-like catalyst: mechanism and efficiency, *Chem. Eng. J.* 357 (2019) 337–347.
- [9] Y. Zhen, S. Zhu, Z. Sun, Y. Tian, Z. Li, C. Yang, J. Ma, Identifying the persistent free radicals (PFRs) formed as crucial metastable intermediates during peroxymonosulfate (PMS) activation by N-doped carbonaceous materials, *Environ. Sci. Technol.* 55 (2021) 9293–9304.
- [10] J.L. Wang, H. Chen, Catalytic ozonation for water and wastewater treatment: recent advances and perspective, *Sci. Total. Environ.* 704 (2020), 135249.
- [11] Y. Zhao, S.X. Chen, H. Qie, S.S. Zhu, C.Y. Zhang, X.Y. Li, W. Wang, J. Ma, Z.Q. Sun, Selective activation of peroxymonosulfate govern by B-site metal in delafossite for efficient pollutants degradation: pivotal role of d orbital electronic configuration, *Water Res.* 236 (2023), 119957.
- [12] W. Hong, Y. Liu, T. Zhu, H. Wang, Y. Sun, F. Shen, X. Li, Promoting the catalytic ozonation of toluene by introducing SO₄²⁻ into the α -MnO₂/ZSM-5 catalyst to tune both oxygen vacancies and acid sites, *Environ. Sci. Technol.* 448 (2022), 130900.
- [13] L. Yang, C. Hu, Y. Nie, J. Qu, Surface acidity and reactivity of β -FeOOH/Al₂O₃ for pharmaceuticals degradation with ozone: in situ ATR-FTIR studies, *Appl. Catal. B Environ.* 97 (2010) 340–346.
- [14] S. Tan, T. Huang, I. Yavuz, R. Wang, T.W. Yoon, M. Xu, Q. Xing, K. Park, D.-K. Lee, C.-H. Chen, R. Zheng, T. Yoon, Y. Zhao, H.-C. Wang, D. Meng, J. Xue, Y.J. Song, X. Pan, N.-G. Park, J.-W. Lee, Y. Yang, Stability-limiting heterointerfaces of perovskite photovoltaics, *Nature* 605 (2022) 268–273.
- [15] D. Avnir, Recent progress in the study of molecularly doped metals, *Adv. Mater.* 30 (2018), 1706804.
- [16] Y. Zhao, G. Chen, T. Bian, C. Zhou, G.I.N. Waterhouse, L.-Z. Wu, C.-H. Tung, L. J. Smith, D. O'Hare, T. Zhang, Defect-rich ultrathin ZnAl-layered double hydroxide nanosheets for efficient photoreduction of CO₂ to CO with water, *Adv. Mater.* 27 (2015) 7824–7831.
- [17] Y. Bu, H. Li, W. Yu, Y. Pan, L. Li, Y. Wang, L. Pu, J. Ding, G. Gao, B. Pan, Peroxydisulfate activation and singlet oxygen generation by oxygen vacancy for degradation of contaminants, *Environ. Sci. Technol.* 55 (2021) 2110–2120.
- [18] Y. Wang, L. Chen, H. Cao, Z. Chi, C. Chen, X. Duan, Y. Xie, F. Qi, W. Song, J. Liu, S. Wang, Role of oxygen vacancies and Mn sites in hierarchical Mn₂O₃/LaMnO_{3-s} perovskite composites for aqueous organic pollutants decontamination, *Appl. Catal. B Environ.* 245 (2019) 546–554.
- [19] S.B. Hammouda, C. Salazar, F. Zhao, D.L. Ramasamy, E. Laklova, S. Iftikhar, I. Babu, M. Sillanpää, Efficient heterogeneous electro-Fenton incineration of a contaminant of emergent concern-cotinine-in aqueous medium using the magnetic double perovskite oxide Sr₂FeCuO₆ as a highly stable catalyst: degradation kinetics and oxidation products, *Appl. Catal. B Environ.* 240 (2019) 201–214.
- [20] J. Bao, X. Zhang, B. Fan, J. Zhang, M. Zhou, W. Yang, X. Hu, H. Wang, B. Pan, Y. Xie, Ultrathin spinel-structured nanosheets rich in oxygen deficiencies for enhanced electrocatalytic water oxidation, *Angew. Chem. Int. Ed.* 54 (2015) 7399–7404.
- [21] L. Wu, Z. Sun, Y. Zhen, S. Zhu, C. Yang, J. Lu, Y. Tian, D. Zhong, J. Ma, Oxygen vacancy-induced nonradical degradation of organics: critical trigger of oxygen (O₂) in the Fe-Co LDH/peroxymonosulfate system, *Environ. Sci. Technol.* 55 (2021) 15400–15411.
- [22] L. Liu, Q. Liu, Y. Wang, J. Huang, W. Wang, L. Duan, X. Yang, X. Yu, X. Han, N. Liu, Nonradical activation of peroxydisulfate promoted by oxygen vacancy-laden NiO for catalytic phenol oxidative polymerization, *Appl. Catal. B Environ.* 254 (2019) 166–173.

- [23] H. Zhang, C. Li, L. Lyu, C. Hu, Surface oxygen vacancy inducing peroxymonosulfate activation through electron donation of pollutants over cobalt-zinc ferrite for water purification, *Appl. Catal. B Environ.* 270 (2020), 118874.
- [24] H.S. Kim, J.B. Cook, H. Lin, J.S. Ko, S.H. Tolbert, V. Ozolins, B. Dunn, Oxygen vacancies enhance pseudocapacitive charge storage properties of MoO_{3-x} , *Nat. Mater.* 16 (2017) 454–460.
- [25] J. Wan, X. Yao, X. Gao, X. Xiao, T. Li, J. Wu, W. Sun, Z. Hu, H. Yu, L. Huang, M. Liu, J. Zhou, Microwave combustion for modification of transition metal oxides, *Adv. Funct. Mater.* 26 (2016) 7263–7270.
- [26] X. Xie, Y. Li, Z.-Q. Liu, M. Haruta, W. Shen, Low-temperature oxidation of CO catalysed by Co_3O_4 nanorods, *Nature* 458 (2009) 746–749.
- [27] C. He, Y. Wang, Z. Li, Y. Huang, Y. Liao, D. Xia, S. Lee, Facet engineered α - MnO_2 for efficient catalytic ozonation of odor CH_3SH : oxygen vacancy-induced active centers and catalytic mechanism, *Environ. Sci. Technol.* 54 (2020) 12771–12783.
- [28] P. Han, H. Lv, X. Li, S. Wang, Z. Wu, X. Li, Z. Mu, X. Li, C. Sun, H. Wei, L. Ma, Perovskite CaZrO_3 for efficient ozonation treatment of organic pollutants in wastewater, *Catal. Sci. Technol.* 11 (2021) 3697–3705.
- [29] H.G. Yang, C.H. Sun, S.Z. Qiao, J. Zou, G. Liu, S.C. Smith, H.M. Cheng, G.Q. Lu, Anatase TiO_2 single crystals with a large percentage of reactive facets, *Nature* 453 (2008) 638–641.
- [30] X. Lin, S. Li, H. He, Z. Wu, J. Wu, L. Chen, D. Ye, M. Fu, Evolution of oxygen vacancies in MnO_x - CeO_2 mixed oxides for soot oxidation, *Appl. Catal. B Environ.* 223 (2018) 91–102.
- [31] Y. Wang, J. Cai, M. Wu, J. Chen, W. Zhao, Y. Tian, T. Ding, J. Zhang, Z. Jiang, X. Li, Rational construction of oxygen vacancies onto tungsten trioxide to improve visible light photocatalytic water oxidation reaction, *Appl. Catal. B Environ.* 239 (2018) 398–407.
- [32] Z. Su, W. Yang, C. Wang, S. Xiong, X. Cao, Y. Peng, W. Si, Y. Weng, M. Xue, J. Li, Roles of oxygen vacancies in the bulk and surface of CeO_2 for toluene catalytic combustion, *Environ. Sci. Technol.* 54 (2020) 12684–12692.
- [33] G. Kresse, J. Furthmüller, Efficient iterative schemes for ab initio total-energy calculations using a plane-wave basis set, *Phys. Rev. B* 54 (1996) 11169–11186.
- [34] G. Kresse, J. Furthmüller, Efficiency of ab-initio total energy calculations for metals and semiconductors using a plane-wave basis set, *Comput. Mater. Sci.* 6 (1996) 15–50.
- [35] J.P. Perdew, J.A. Chevary, S.H. Vosko, K.A. Jackson, M.R. Pederson, D.J. Singh, C. Fiolhais, Atoms, molecules, solids, and surfaces: applications of the generalized gradient approximation for exchange and correlation, *Phys. Rev. B* 46 (1992) 6671–6687.
- [36] J.P. Perdew, K. Burke, M. Ernzerhof, Generalized gradient approximation made simple, *Phys. Rev. Lett.* 77 (1996) 3865–3868.
- [37] G. Zhu, J. Zhu, W. Jiang, Z. Zhang, J. Wang, Y. Zhu, Q. Zhang, Surface oxygen vacancy induced α - MnO_2 nanofiber for highly efficient ozone elimination, *Appl. Catal. B Environ.* 209 (2017) 729–737.
- [38] S. Rong, P. Zhang, F. Liu, Y. Yang, Engineering crystal facet of α - MnO_2 nanowire for highly efficient catalytic oxidation of carcinogenic airborne formaldehyde, *ACS Catal.* 8 (2018) 3435–3446.
- [39] J. Jiang, X. Wang, Q. Xu, Z. Mei, L. Duan, H. Guo, Understanding dual-vacancy heterojunction for boosting photocatalytic CO_2 reduction with highly selective conversion to CH_4 , *Appl. Catal. B Environ.* 316 (2022), 121679.
- [40] J. Hou, Y. Li, M. Mao, L. Ren, X. Zhao, Tremendous effect of the morphology of birnessite-type manganese oxide nanostructures on catalytic activity, *ACS Appl. Mater. Interfaces* 6 (2014) 14981–14987.
- [41] F.X. Tian, H. Li, M. Zhu, W. Tu, D. Lin, Y.F. Han, Effect of MnO_2 polymorphs' structure on low-temperature catalytic oxidation: crystalline controlled oxygen vacancy formation, *ACS Appl. Mater. Interfaces* 14 (2022) 18525–18538.
- [42] M. Guo, J. Lu, Y. Wu, Y. Wang, M. Luo, UV and visible Raman studies of oxygen vacancies in rare-earth-doped ceria, *Langmuir* 27 (2011) 3872–3877.
- [43] Y.T. Chua, P.C. Stair, I.E. Wachs, A comparison of ultraviolet and visible Raman spectra of supported metal oxide catalysts, *J. Phys. Chem. B* 105 (2001) 8600–8606.
- [44] Y. Guo, J. Long, J. Huang, G. Yu, Y. Wang, Can the commonly used quenching method really evaluate the role of reactive oxygen species in pollutant abatement during catalytic ozonation? *Water Res.* 215 (2022), 118275.
- [45] F. Nawaz, H. Cao, Y. Xie, J. Xiao, Y. Chen, Z.A. Ghazi, Selection of active phase of MnO_2 for catalytic ozonation of 4-nitrophenol, *Chemosphere* 168 (2017) 1457–1466.
- [46] K. Yaghmaei, G. Moussavi, A. Mashayekh-Salehi, A. Mohseni-Bandpei, M. Satari, Oxidation of acetaminophen in the ozonation process catalyzed with modified MgO nanoparticles: effect of operational variables and cytotoxicity assessment, *Process Saf. Environ. Prot.* 109 (2017) 520–528.
- [47] S. Zhu, B. Dong, Y. Yu, L. Bu, J. Deng, S. Zhou, Heterogeneous catalysis of ozone using ordered mesoporous Fe_3O_4 for degradation of atrazine, *Chem. Eng. J.* 328 (2017) 527–535.
- [48] Z. He, A. Zhang, S. Song, Z. Liu, J. Chen, X. Xu, W. Liu, γ - Al_2O_3 modified with praseodymium: an application in the heterogeneous catalytic ozonation of succinic acid in aqueous solution, *Ind. Eng. Chem. Res.* 49 (2010) 12345–12351.
- [49] F.J. Beltrán, F.J. Rivas, R. Montero-de-Espinosa, Catalytic ozonation of oxalic acid in an aqueous TiO_2 slurry reactor, *Appl. Catal. B Environ.* 39 (2002) 221–231.
- [50] G.D. Fang, D.D. Dionysiou, S.R. Al-Abed, D.M. Zhou, Superoxide radical driving the activation of persulfate by magnetite nanoparticles: implications for the degradation of PCBs, *Appl. Catal. B Environ.* 129 (2013) 325–332.
- [51] B.A. Lindig, M. Rodgers, A.P. Schaap, Determination of the lifetime of singlet oxygen in D_2O using 9,10-anthracenedipropionic acid, a water-soluble probe, *J. Am. Chem. Soc.* 102 (1980) 5590–5593.
- [52] Z. Sun, L. Zhao, C. Liu, Y. Zhen, J. Ma, Catalytic ozonation of ketoprofen with in situ N-doped carbon: a novel synergetic mechanism of hydroxyl radical oxidation and an intra-electron-transfer nonradical reaction, *Environ. Sci. Technol.* 53 (2019) 10342–10351.
- [53] Z. Wang, W. Wang, J. Wang, Y. Yuan, Q. Wu, H. Hu, High-valent iron-oxo species mediated cyclic oxidation through single-atom Fe-N_6 sites with high peroxymonosulfate utilization rate, *Appl. Catal. B Environ.* 305 (2022), 121049.
- [54] L. Tang, Y. Liu, J. Wang, G. Zeng, Y. Deng, H. Dong, H. Feng, J. Wang, B. Peng, Enhanced activation process of persulfate by mesoporous carbon for degradation of aqueous organic pollutants: electron transfer mechanism, *Appl. Catal. B Environ.* 231 (2018) 1–10.
- [55] G. Fang, J. Gao, C. Liu, D.D. Dionysiou, Y. Wang, D. Zhou, Key role of persistent free radicals in hydrogen peroxide activation by biochar: implications to organic contaminant degradation, *Environ. Sci. Technol.* 48 (2014) 1902–1910.
- [56] R. Zeng, C. Cheng, F. Xing, Y. Zou, K. Ding, C. Huang, Dual vacancies induced local polarization electric field for high-performance photocatalytic H_2 production, *Appl. Catal. B Environ.* 316 (2022), 121680.
- [57] S.S. Sable, P.P. Ghute, D. Fakhraasova, R.B. Mane, C.V. Rode, F. Medina, S. Contreras, Catalytic ozonation of clofibric acid over copper-based catalysts: in situ ATR-IR studies, *Appl. Catal. B Environ.* 209 (2017) 523–529.
- [58] F. Fang, N. Feng, L. Wang, J. Meng, G. Liu, P. Zhao, P. Gao, J. Ding, H. Wan, G. Guan, Fabrication of perovskite-type macro/mesoporous $\text{La}_{1-x}\text{K}_x\text{FeO}_{3-\delta}$ nanotubes as an efficient catalyst for soot combustion, *Appl. Catal. B Environ.* 236 (2018) 184–194.
- [59] G. Zhai, S. Liu, S. Si, Y. Liu, H. Zhang, Y. Mao, M. Zhang, Z. Wang, H. Cheng, P. Wang, Z. Zheng, Y. Dai, B. Huang, Oxygen vacancies enhanced ozonation toward phenol derivatives removal over O_v - Bi_2O_3 , *ACS ES&T, Water* 2 (2022) 1725–1733.
- [60] X. Dong, X. Duan, Z. Sun, X. Zhang, C. Li, S. Yang, B. Ren, S. Zheng, D.D. Dionysiou, Natural illite-based ultrafine cobalt oxide with abundant oxygen-vacancies for highly efficient Fenton-like catalysis, *Appl. Catal. B Environ.* 261 (2020) 118–124.
- [61] C. Mansas, J. Mendret, S. Brosillon, A. Ayral, Coupling catalytic ozonation and membrane separation: a review, *Sep. Purif. Technol.* 236 (2020), 116221.
- [62] L. Wu, Z. Li, P. Cheng, Y. She, W. Wang, Y. Tian, J. Ma, Z. Sun, Efficient activation of peracetic acid by mixed sludge derived biochar: critical role of persistent free radicals, *Water Res.* 223 (2022), 119013.